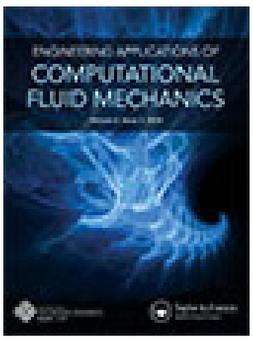

Taylor & Francis
Taylor & Francis Group

Engineering Applications of Computational Fluid Mechanics

ISSN: 1994-2060 (Print) 1997-003X (Online) Journal homepage: https://www.tandfonline.com/loi/tcfm20

CFD Study of Drag Reduction in Axisymmetric Underwater Vehicles using Air Jets

S. G. Shereena, S. Vengadesan, V. G. Idichandy & S. K. Bhattacharyya

To cite this article: S. G. Shereena, S. Vengadesan, V. G. Idichandy & S. K. Bhattacharyya (2013) CFD Study of Drag Reduction in Axisymmetric Underwater Vehicles using Air Jets, Engineering Applications of Computational Fluid Mechanics, 7:2, 193-209, DOI: 10.1080/19942060.2013.11015464

To link to this article: https://doi.org/10.1080/19942060.2013.11015464

Published online: 19 Nov 2014.

Engineering Applications of Computational Fluid Mechanics Vol. 7, No. 2, pp. 193–209 (2013)

CFD STUDY OF DRAG REDUCTION IN AXISYMMETRIC UNDERWATER VEHICLES USING AIR JETS

Shereena S. G. *, S. Vengadesan [#†], V. G. Idichandy * and S. K. Bhattacharyya *

* *Department of Ocean Engineering, Indian Institute of Technology Madras, Chennai 600036, India*
[#] *Department of Applied Mechanics, Indian Institute of Technology Madras, Chennai 600036, India*
[†] *E-Mail: vengades@iitm.ac.in* (*Corresponding Author*)

ABSTRACT: A computational fluid dynamics approach to study drag reduction of axisymmetric underwater bodies by air jet injection in the boundary layer is presented. The well-known 'mixture' model is used to capture the multiphase flow and the SST k-ω (shear stress transport) turbulence closure model has been used in the computations. Well-studied Afterbody1 (Huang et al., 1978) which has a tapered and smooth stern profile is considered. A companion shape of Afterbody1, which has a blunt stern profile, is also studied. The numerical study is carried out with different air jet velocity to body velocity ratios, various angles of air jet and various angles of attack of the body. Effects of these parameters on drag reduction are reported. The effect of tapered vs. blunt aft shape of Afterbody1 has been found to have significant effect on drag reduction performance.

Keywords: underwater vehicle, axisymmetric body, computational fluid dynamics, air jet, drag reduction

1. INTRODUCTION

Turbulent flows can occur in the boundary layer near solid surfaces. The energy losses and self-noise due to turbulence can be of very high magnitude. It can affect the performance of many engineering devices. This necessitates unabated research on strategies for drag reduction. One of the ways to achieve drag reduction is to delay the onset of turbulent flow, which a drag reducer does by shifting the transition from laminar to turbulent flow to a higher flow velocity.

Important drag reduction technologies reported in literature are introduction of polymers, surfactants and microbubbles in the boundary layer and use of compliant coatings on the surface. Gas-based drag reduction technologies include supercavitation, partial cavitation and microbubble ejection. Microbubbles are perhaps the cheapest and the most non-polluting drag reducer where air bubbles are introduced to reduce the frictional resistance. The injected air bubbles modify the energy inside a turbulent boundary layer and thereby lower the skin friction. However, the control of the bubble size and the angle of ejection can impose technical challenges. Introduction of air jets in the boundary layer also gives similar drag reduction effects as that of microbubbles. In the present study, drag reduction is obtained by ejecting air jets in the boundary layer. In both methods, the major reason of drag reduction is due to reduction in molecular viscosity of fluid along the length of the body. By introducing air jets or microbubbles, the frictional component of drag force is greatly reduced. The use of air jets retains the advantage of being the cheapest non-polluting drag reducer as well as those using microbubbles.

In this work, the Reynolds-Averaged Navier-Stokes (RANS) equations, commonly used in Computational Fluid Dynamics (CFD) techniques for studying different practical flows are used to study the drag reduction of axisymmetric underwater vehicles using air jets.

2. LITERATURE

A number of drag reduction studies have been done on flat plates as well as on axisymmetric bodies. In a review, Truong (2001) has discussed some of the important drag reduction technologies such as introduction of polymers, surfactants, microbubbles and compliant coatings on the wall surface. Madavan et al. (1985 and 1984) used an array of flush-mounted hot films to study the downstream evolution and persistence of the reduction of skin friction in the microbubble-laden turbulent boundary layer over a flat plate. Kim and Cleaver (1995) considered experimental data to investigate the way in which the reduction in wall shear stress changes with distance from the microbubble injection region. Kato et al. (1999) measured velocity and turbulence intensity of a turbulent boundary layer with microbubbles by a Laser Doppler Velocimeter (LDV) system in forward scatter mode for flow over a flat plate.

Received: 15 Jan. 2012; Revised: 30 Oct. 2012; Accepted: 23 Nov. 2012

Kodama et al. (2000) experimentally studied microbubbles using a specially designed circulating water tunnel. Moriguchi and Kato (2002) examined the effect of microbubbles on drag reduction in a two-dimensional (2D) flow channel with the aim of clarifying effect of bubble size. Wedin et al. (2003) conducted an experimental investigation of microbubble flow within a vertical pipe. Hassan et al. (2005) studied the structure of flow turbulence in a water channel with microbubbles using Particle Image Velocimetry (PIV) at a Reynolds number of 5128. Wu et al. (2005) analysed the interaction between liquid turbulent boundary layer and a crowded group of microbubbles. Murai et al. (2007) experimentally investigated skin friction drag reduction in a horizontal rectangular channel by bubbles that are large relative to the shear layer. Wu et al. (2008) attempted to find the optimum parameters for robust design of the microbubble drag reduction in turbulent channel flow.

Deutsch and Castano (1985) studied the injection of gas to form microbubbles in turbulent boundary layer in water tunnel tests to reduce skin friction drag on an axisymmetric body. Fontaine and Deutsch (1992) studied the influence of the type of gas on the performance of microbubble skin friction reduction on an axisymmetric body. The gases used were of different density and solubility such as air, helium, carbon dioxide and argon. Helium was found to be more effective than other gases. Wu et al. (2006) numerically simulated the effect of microbubble flow around an axisymmetric body. They found that around 50% of drag reduction can be obtained by injecting microbubbles into the flow with most favorable combination of parameters. John et al. (2011) carried out an interesting study of drag reduction in emperor penguins who release air from their bodies. Xiang et al. (2011) studied the turbulent bubbly wakes formed downstream of an axisymmetric body, which gives an in depth understanding of complex multiphase ventilated partial cavity situations.

Various numerical studies have been done to calculate drag force and drag reduction using microbubbles. Kanai and Miyata (2001) developed a marker density function method to conduct Direct Numerical Simulation (DNS) for bubbly flows. Skudarnov and Lin (2006) found that a single phase model with bubbles introduced as a species mass source was able to predict drag reduction more consistent with the experimental data than that by a more complex two-fluid model. Mohanarangam et al. (2009) studied the phenomenon of drag reduction by the injection of microbubbles into a turbulent boundary layer using an Eulerian-Eulerian two-fluid model. Ali et al. (2010) studied drag reduction in ships using air lubrication. They have done CFD studies on flat plate which was equivalent to the wetted surface of the ship. Higher drag reduction was reported in the case of low Froude number of the ship and high air flow velocities.

From the literature review, it is observed that lowering the viscosity of fluid along the length of the body using microbubbles is an effective method of drag reduction. Introducing air jets to the surface of the body will also reduce viscosity of fluid along the body length. Hence a similar approach can be used to study drag reduction using air jets.

Mohanarangam et al. (2009) and Wu et al. (2006) suggested that the SST k-ω model is best suited to capture turbulence in RANS based CFD approach for two phase flow in this class of problems. Hence this turbulence model is used in the present CFD study.

3. PROBLEM DESCRIPTION

In this work, for the purpose of limited validation alone, an axisymmetric body (Fig. 1) considered by Wu et al. (2006) in a CFD study of drag reduction using microbubbles has been adopted. They studied the distribution of microbubbles around the body and the drag reduction of the body under different conditions, such as using bubbles of different diameters, different body velocities and bubble ejection rates. They reported a maximum of 50% drag reduction and in the present work 44.8% of drag reduction was obtained for the same case (Table 1).

For the detailed CFD study of drag reduction using air jets, two axisymmetric underwater vehicle shapes have been chosen. These body shapes are designated as Afterbody1 (Fig. 2) and Blunt Afterbody1 (Fig. 3). The geometry of Afterbody1 is given by Huang et al. (1978). In this work, an extensive experimental wind tunnel study on this body shape is reported covering detailed measurements of static pressure distribution, mean velocity profiles and distributions of turbulence intensities and Reynolds stress across the stern boundary layers; however, the Reynolds number was held constant (6.6×10^6).This body shape was numerically studied by Sarkar et al. (1997) using four different turbulence models. They found that standard k-ε model with wall function predicted the flow characteristics more accurately than the other

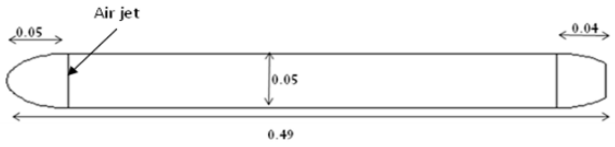

Fig. 1 Geometry of axisymmetric body (from Wu et al., 2006) showing air jet ring (dimensions in m).

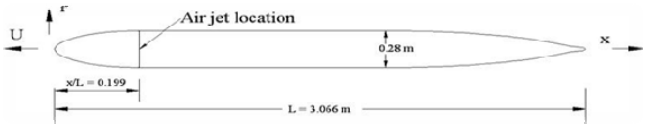

Fig. 2 Geometry of Afterbody1 (Huang et al., 1978) showing air jet ring.

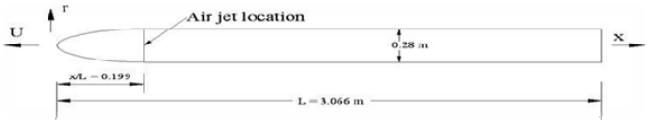

Fig. 3 Geometry of Blunt Afterbody1 showing air jet ring.

models. Jagadeesh and Murali (2006) also studied a variety of turbulence models for this geometry.

The geometry of Blunt Afterbody1 is same as that of Afterbody1 in the nose and parallel middle body region as also in total length. In Blunt Afterbody1, the parallel middle body extends the full length and ends there without any streamlined tapering of the stern (aft) profile as in Afterbody1. Since base drag is expected to be a significant component of the total drag of the Blunt Afterbody1, its drag reduction characteristics is expected to be significantly different from that of Afterbody1.

The location of the air jet is chosen at the shoulder of the nose shape (Figs. 2 and 3), where the parallel middle body (i.e. $r = R$) starts. The preferred angle of the air jet with the x-axis (θ) is 30° for the study of effect of air jet velocity to body velocity. For studying the effect of the angle of injection of air jet, however, five angles are used (θ = 10°, 20°, 30°, 60° and 90°). Axisymmetric CFD calculations are made use of; therefore the implied shape of the air jet is a circular ring. For studying the effect of the angle of attack (α) of the flow with respect to the body, a three-dimensional (3D) CFD simulation is done with four discrete air jets, each 90° apart, with the same total mass flow rate as the axisymmetric studies having a ring shaped air jet. Its size (i.e. in the length direction) is maintained for the ring jet and discrete jet geometries. For various air jet velocity (U_{jet}) to body velocity (U) ratios, drag reduction calculations are carried out. Commercially available CFD software FLUENT has been used for all simulations.

4. NUMERICAL STRATEGIES

The basic fluid needs only single phase simulation, i.e. water. However, when the air jet is introduced, the flow becomes two phase flow. For simulating two phase flow, the 'mixture' model, as implemented in FLUENT, is used. This can be used to model multiphase flow where the phases move at different velocities. The mixture model can model 'n' phases (fluid or particulate) by solving the momentum and continuity for the mixture, the volume fraction equations for the secondary phases, and the algebraic expressions for the relative velocities. The phases are treated as 'interpenetrating' continua. An extensive discussion on this model may be found in Manninen et al (1996), where other references on this and various other two-phase models may also be found.

4.1 Governing equations

The continuity equation for the mixture (m) is

$$\frac{\partial \rho_m}{\partial t} + \rho_m \vec{v}_m = 0 \tag{1}$$

where ρ_m is the mixture density, t is time and $\vec{v}_m$ is the mass averaged velocity given. The mixture density and mass averaged velocity are given by

$$\rho_m = \sum_{k=1}^{n} \alpha_k \rho_k \tag{2}$$

$$\vec{v}_m = \frac{\sum_{k=1}^{n} \alpha_k \rho_k \vec{v}_k}{\rho_m} \tag{3}$$

where α_k is the volume fraction (VF) of phase k, ρ_k is its density and $\vec{v}_k$ is the mass averaged velocity of this phase. The momentum equation of the mixture is obtained by summing the individual momentum equations for all phases. It can be expressed as

$$\begin{aligned} &\frac{\partial}{\partial t}\left(\rho_m \vec{v}_m\right) + \nabla \cdot \left(\rho_m \vec{v}_m \cdot \vec{v}_m\right) = \\ &-\nabla p + \nabla \cdot \left[\mu_m \left(\nabla \vec{v}_m + \nabla \vec{v}_m^T \vec{v}_m^T\right)\right] \\ &+\rho_m g + \vec{F} + \nabla \cdot \left(\sum_{k=1}^{n} \alpha_k \rho_k \vec{v}_{dr,k} \vec{v}_{dr,k}\right) \end{aligned} \tag{4}$$

where p is pressure, g is the acceleration due to gravity, $\vec{F}$ is a body force intensity and μ_m is the viscosity of the mixture given by

$$\mu_m = \sum_{k=1}^{n} \alpha_k \mu_k \tag{5}$$

$\vec{v}_{dr,k}$ is the drift velocity for secondary phase k, defined as $\vec{v}_{dr,k} = \vec{v}_k - \vec{v}_m$ and μ_k is the viscosity of this phase. The relative velocity (also referred to as the slip velocity) is defined as the velocity of a secondary phase (p) relative to the velocity of the primary phase (q)

$$\vec{v}_{pq} = \vec{v}_p - \vec{v}_q \tag{6}$$

The mass fraction of any phase (k) is defined as

$$c_k = \frac{\alpha_k \rho_k}{\rho_m} \tag{7}$$

The drift velocity and the relative velocity $\vec{v}_{pq}$ are connected by

$$\vec{v}_{dr,p} = \vec{v}_{pq} - \sum_{k=1}^{n} c_k \vec{v}_{qk} \tag{8}$$

The mixture model makes use of an algebraic slip formulation. The basic assumption of the algebraic slip mixture model is to prescribe an algebraic relation for the relative velocity, a local equilibrium between the phases should be reached over short spatial length scale.

From the continuity equation for the secondary phase p, the VF equation for secondary phase p is obtained as

$$\frac{\partial}{\partial t}\left(\alpha_p \rho_p\right) + \nabla.\left(\alpha_p \rho_p v_m\right) = -\nabla.\left(\alpha_p \rho_p \vec{v}_{dr,p}\right) + \sum_{q=1}^{n}\left(in_{qp} - in_{pq}\right) \tag{9}$$

where $\dot{m}_{qp}$ and $\dot{m}_{pq}$ are the mass flow rates.

For simulating turbulent flow, the SST k-ω turbulence model is used in calculations based on the recommendation of Mohanarangam et al. (2009) and Wu et al. (2006), who found that this model is well suited for simulating two phase flows. This model is an effective blend of robust and accurate formulation of the k-ω model in the near wall region and k-ε model in the far field.

4.2 Computational domain and boundary conditions

Symmetry of the problem is exploited by adopting an axisymmetric domain in a plane as shown in Fig. 4. The domain details and boundary conditions are taken from Virag et al. (2011). The boundary conditions are: (a) segment AB is a velocity inlet, i.e. where U is prescribed in the x direction; (b) segment CD is the pressure outlet where the gradients of turbulent kinetic energy (k of SST k-ω model) and dissipation rate (ω of SST k-ω model) are set to zero and the pressure is set to the gauge pressure i.e. $p = 0$; (c) segment AD is the cylindrical surface where zero shear stress is prescribed; (d) symmetry conditions are prescribed on x-axis given by the segment BC and (e) no slip condition is prescribed on the body surface (or wall). Standard wall functions are used to calculate the variables at the near-wall cells. At a distance of X_{jet} from the nose of the body, air jet is introduced at an angle of θ (Figs. 4 and 5). The boundary condition used is a velocity inlet with air velocity of U_{jet}.

At the velocity inlet (segment AB), one needs to specify a representative value of turbulent intensity parameter T_u and length scale l. In all calculations, the values of these parameters have been chosen as T_u= 0.05 (i.e. 5 %) and l = 0.001L, where L is the length of the body.

For 3D simulations, the same boundary conditions are used with four discrete air jets.

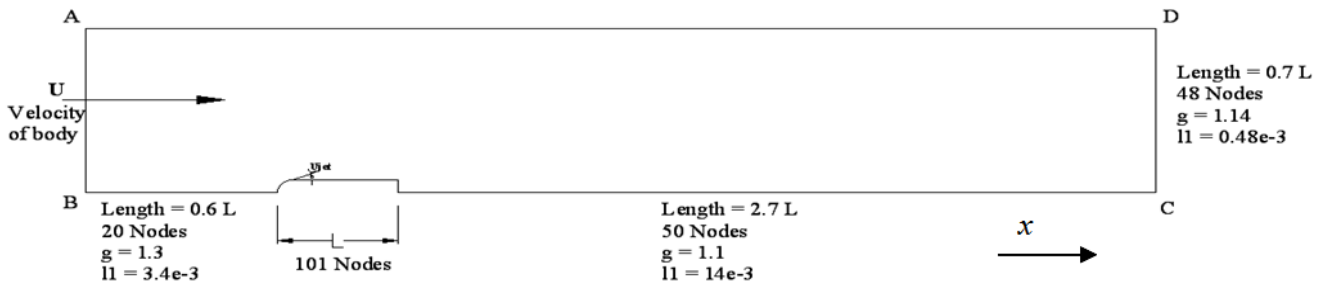

Fig. 4 Computational domain.

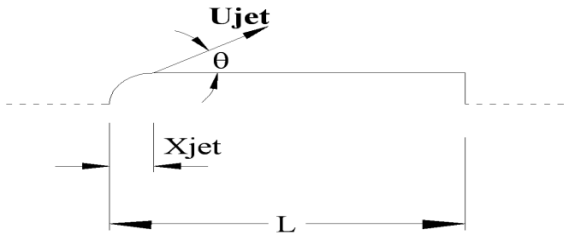

Fig. 5 Enlarged view of domain details on body.

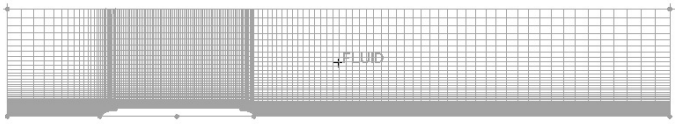

(a) Mesh over the domain

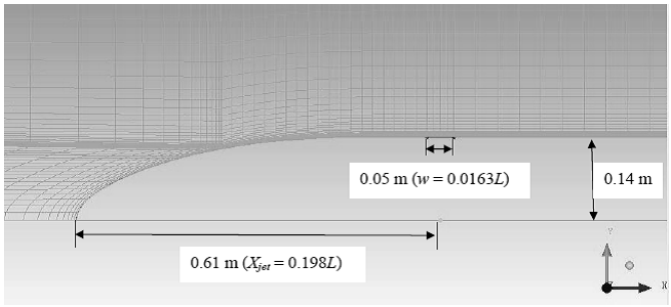

(b) Mesh near location of air jet and air inlet size

Fig. 6 2D axisymmetric mesh for Afterbody1.

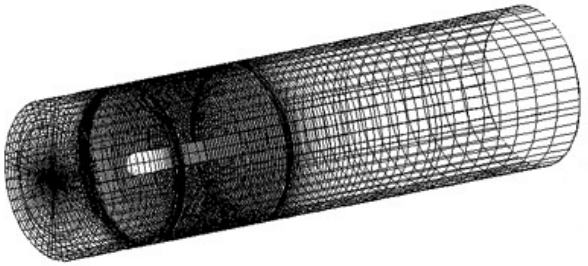

(a) Zero angle of attack (No. of nodes = 253798; No. of elements = 248000)

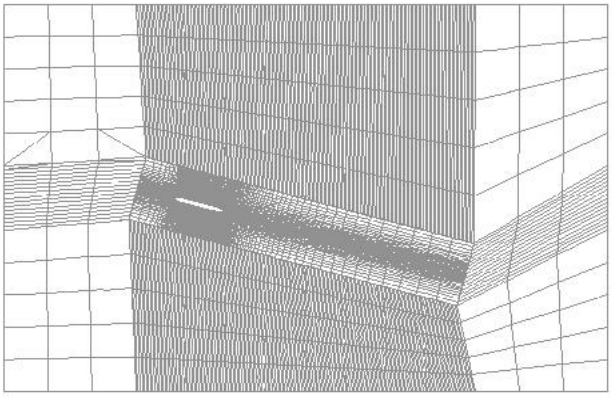

(b) 15 deg. angle of attack (No. of nodes = 567822; No. of elements = 544960)

Fig. 7 3D mesh for Afterbody1.

4.3 Grid and discretization

A sample of axisymmetric mesh is shown in Fig. 6 and two samples of 3D meshes are shown in Fig. 7, one for zero angle of attack and one for nonzero angle of attack. Let the grid point nearest to the body surface be located at a radial distance of l_1 from the body surface (or near wall spacing) and let the growth ratio (g) be defined as ratio of successive distances between grid points normal to the body surface. This means that length of the Nth cell away from the body surface in the normal direction, l_N, is given by $l_N = l_1 g^{N-1}$ and the total length of N cells will be given by $\sum_{i=1}^{N} l_1 g^{i-1}$.

For the SST k-ω model, 'near wall' is treated in the same way as in the k-ε model. In the k-ε model, for the wall law to be applicable, the grid size should be adjusted such that $30 \le y^+ \le 300$, and the wall adjacent cells are not placed in the buffer layer of $y^+ = 5$ to 30.The growth ratio is so designed that it prevents the wall adjacent cells from being placed in the buffer layer. In this, y^+ (sometimes called 'wall unit') is given by the formula $y^+ = l_1 u_\tau / \nu$ and $u_\tau = \sqrt{\tau_w / \rho}$ where u_τ is the friction velocity and τ_w is the wall shear stress. The placement of the wall adjacent cells, however, has to be done by trial and error because there is no way to know the distribution of wall shear stress. Hence wall unit values over the body surface will not be known *prior* to doing CFD simulation. The meshes in Figs. 6 and 7 are for Afterbody1, where total number of nodes and elements are recorded. Size of air jet inlet (w) used is 0.0163L at a location of 0.1989L from the nose of the body. The volume fraction of air at the air jet inlet is given as 1. However, the mesh for the body in Fig. 1, which had 10260 nodes and 9983 elements, is not given.

In this work, a second order upwind scheme has been used in all calculations using a pressure based, segregated solver which implements an implicit formulation for unsteady flow problems adopting absolute velocity formulation. All simulations were run using an unsteady segregated solver. The convergence criterion of 10^{-4} is set for velocity components and 10^{-3} for continuity, k, and ω, all being RMS values. The time step used in simulation is 0.0001s, which was found to give accurate results for all velocities. Convergence of the time step and mesh convergence study for this geometry were reported earlier in Virag et al. (2011) and hence

not reproduced here. As far as the 3D mesh was concerned, the mesh configuration in any plane was kept the same as the axisymmetric mesh and found to work very well in that it produces practically identical values of drag forces.

5. RESULTS AND DISCUSSION

5.1 Validation

Wu et al. (2006) conducted a numerical simulation of microbubble flow around an axisymmetric body (Fig. 1) where the flow with microbubbles was treated as mixture flow. They also studied the distribution of microbubbles in the vicinity of the body and the resulting drag reduction under different conditions. They have reported a drag reduction up to 50%. In the present work, the same geometry is adopted and similar simulations were performed for the purpose of validation. The velocity of the body was 12 m/s and the jet was 3.6 m/s with θ = 90°(Fig.5). Since much of vital data such as jet width, turbulent intensity and length scale, along with other solver parameters were not reported in the paper, the validation is somewhat approximate. However, the results show a similar trend in drag reduction (Table 1) with about 10% difference in drag reduction. From this exercise, it was concluded that the 'mixture' model and SST k-ω turbulence model are the appropriate CFD models for this class of problems.

For Afterbody1, drag coefficients without an air jet are compared with other published results in Table 2, showing very good agreement. This validates the choices made regarding the mesh, computational domain and various other solver parameters.

5.2 Results for Afterbody1 and Blunt Afterbody1

The drag coefficients of Afterbody1 and Blunt Afterbody1 are presented in Table 3 for two values of Reynolds number. For the drag reduction study, the body velocity (U) was taken as 15 m/s and the air jet velocity was introduced at an inclination of 30°(θ) to the body surface in all calculations for both bodies. The air jet velocities considered for Afterbody 1 were U_{jet} = 0.1, 0.5, 1, 2.5, 5, 7.5, 15 and 30 m/s and those considered for Blunt Afterbody1 were U_{jet} = 1, 5, 15, 30, 50 and 100 m/s. Reductions in drag force for both the bodies are summarized in Table 4 and Fig. 8.

Table 1 Comparison of drag reduction for axisymmetric body studied by Wu et al. (2006).

U (m/s)	U_{jet} (m/s)	Source	$T_{u\,(\%)}$	F_P (N)	F_F(N)	F_D(N)	Drag Reduction (%)
12	0	Present	0.5	6.2	16.4	22.6	-
			5	10.4	19.1	29.5	-
		Wu et al. (2006)	-	3.898	17.75	21.65	-
12	3.6	Present	5	12.77	3.49	16.26	44.8
		Wu et al. (2006)	-	6.5	4.19	10.7	50

F_P: Pressure (viscous) drag, F_F:Frictional (viscous) drag,
F_D(= F_P + F_F):Total drag

Table 2 Comparison of drag coefficients for Afterbody1 (U = 2.152 m/s, Re = 6.6×10^6).

Source	C_{PV}	C_{FV}	C_{DV}	Error (%)
Huang et al. (1978) Experimental	-	-	0.0276	-
Sarkar et al. (1997) CFD	0.0027	0.0297	0.0324	17.39
Present CFD	0.0024	0.0250	0.0274	–0.72

$(C_{PV}, C_{FV}, C_{DV}) = (F_P, F_F, F_D)/(0.5\rho U^2\nabla^{2/3})$
Body volume ∇ = 0.148 m^3, $Re = UL/\nu$, Body length L = 3.066 m,
Kinematic viscosity of water $\nu = 10^{-6}$m^2/s

Table 3: Drag coefficients for Afterbody1 and Blunt Afterbody1 (SST k-ω model with T_u = 5%).

Reynolds number (U)	Body	C_{PV} (F_P)	C_{FV} (F_F)	C_{DV} (F_D)	Increase in C_{DV} (%)	Increase in drag (%)
6.6×10^6 (2.152 m/s)	Afterbody1	0.0024 (1.538 N)	0.0250 (16.24 N)	0.0274 (17.78 N)	-	-
	Blunt Afterbody1	0.0220 (16.33 N)	0.0256 (19.025 N)	0.0477 (35.35 N)	74	98.8
4.6×10^7 (15 m/s)	Afterbody1	0.0016 (53 N)	0.0186 (589 N)	0.0204 (643 N)	-	-
	Blunt Afterbody1	0.0228 (824 N)	0.019 (684 N)	0.0419 (1508 N)	105	134

Body volume ∇ = 0.148 m^3 (Afterbody1); ∇ = 0.181 m^3 (Blunt Afterbody1)

Table 4 Variation of drag reduction with various air jet velocities: U = 15 m/s (Re = 4.6×10^7), θ= 30°.

U_{jet} (m/s)	F_P (N)		F_F (N)		F_D (N)		Drag Reduction (%)	
	A	B	A	B	A	B	A	B
0	53	824	589	684	643	1508	0	-
0.1	51		441		492		23.4	
0.5	56		193		249.9		61.1	
1	79	890	169	224	249.4	1115	61.2	26.06
2.5	159		147		306		52.4	
5	188	805	141	164	329	969	48.8	35.74
7.5	263		138		401		37.6	
15	457	613	136	149	594	762	7.6	49.46
30	550	539	133	137	684	677	–6.3	55.106
50		525		128		654		56.63
100		727		122		846		43.89

A - Afterbody1; B - Blunt Afterbody1

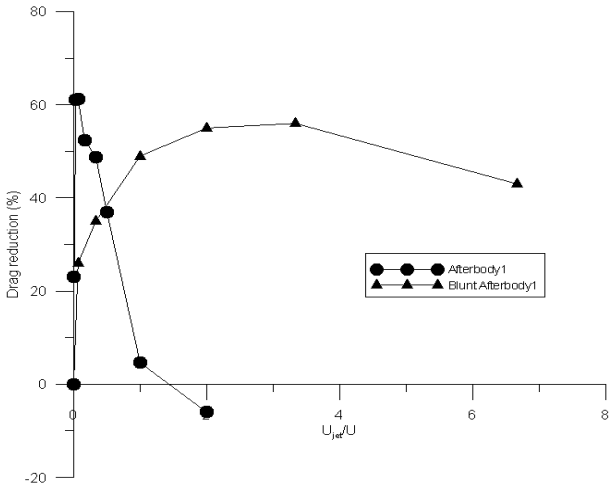

Fig. 8 Comparison of drag reduction for Afterbody1 and Blunt Afterbody1 (θ= 30°).

A contour plot of dynamic pressure around Afterbody1 for U_{jet} = 0 is shown in Fig. 9a and that around Blunt Afterbody1 is shown in Fig. 9b. A contour plot of dynamic pressure around Afterbody1 for the air jet with U_{jet} = 1 m/s (when drag reduction is maximum for Afterbody1) is shown in Fig. 10a and that around Blunt Afterbody1 with U_{jet} = 50 m/s (when drag reduction is maximum for Blunt Afterbody1) is given in Fig. 10b. Contour plots of fluid velocity around Afterbody1 and Blunt Afterbody1 without the air jet are shown in Figs. 11a and 11b, respectively. Contour plots of fluid velocity with the air jet around Afterbody1 (at U_{jet} = 1 m/s) and Blunt Afterbody1 (at U_{jet} = 50 m/s) are shown in Figs. 12a and 12b, respectively. Contour plots of VF of water in the domain for maximum drag reduction for both the bodies are shown in Fig. 13.

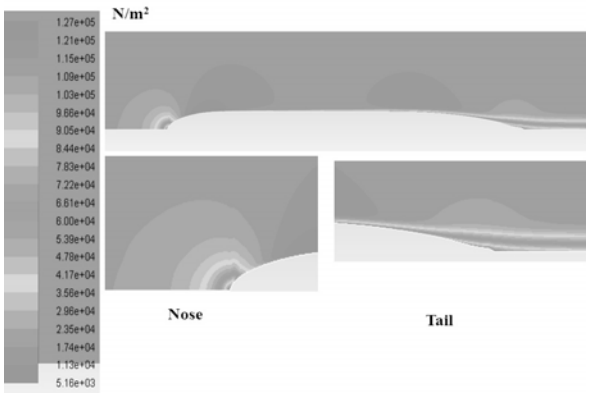

(a) Afterbody1 (U = 15m/s and U_{jet} = 0)

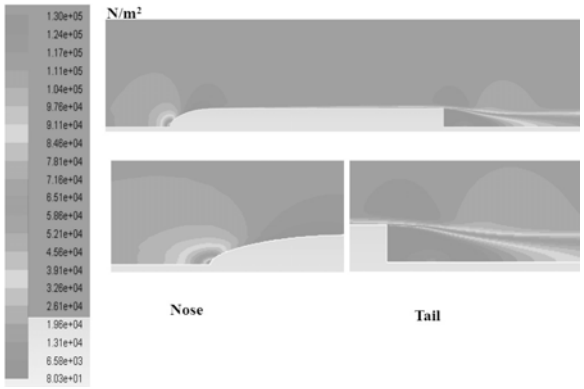

(b) Blunt Afterbody1 (U = 15m/s and U_{jet}= 0)

Fig. 9 Dynamic pressure contours for Afterbody1 and Blunt Afterbody1 without air jet.

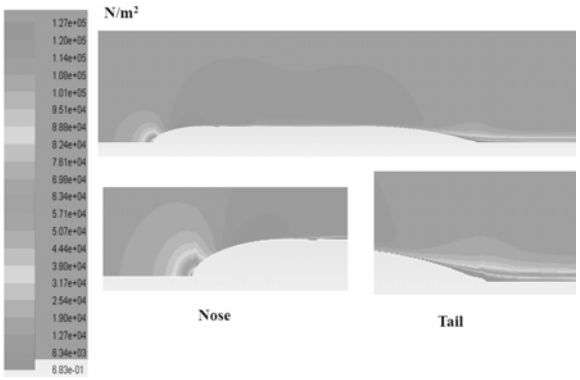

(a) Afterbody1 (U = 15m/s and U_{jet} = 1 m/s)

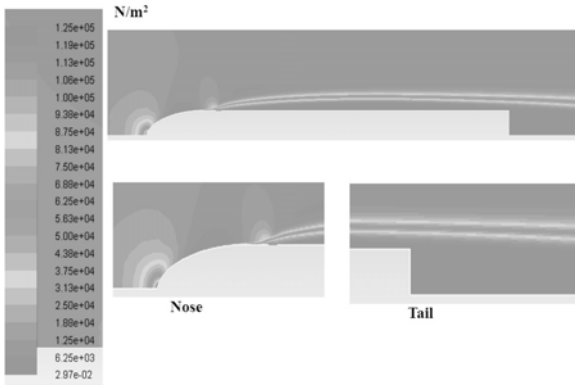

(b) (U = 15m/s and U_{jet} = 50 m/s)

Fig. 10 Dynamic pressure contours for Afterbody1 and Blunt Afterbody1 at air jet speeds corresponding to maximum drag reduction.

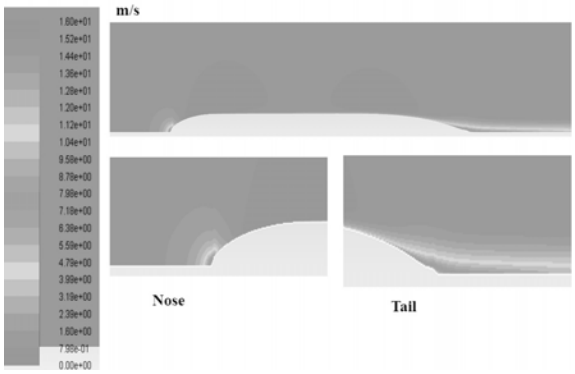

(a) Afterbody1 (U = 15m/s and U_{jet} = 0)

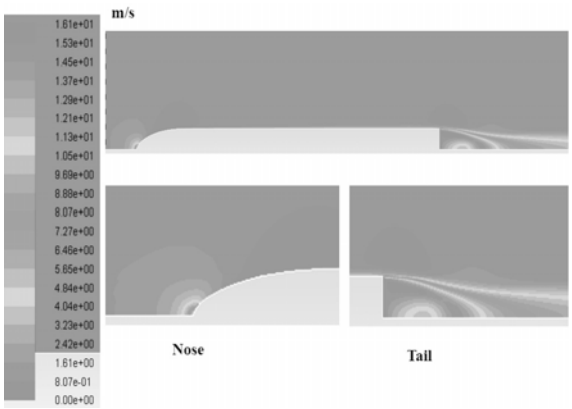

(b) Blunt Afterbody1 (U = 15m/s and U_{jet} = 0)

Fig. 11 Velocity contours for Afterbody1 and Blunt Afterbody1 without air jet.

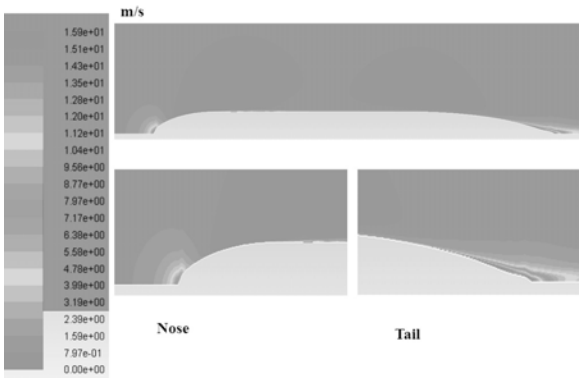

(a) Afterbody1 (U = 15m/s and U_{jet} = 1 m/s)

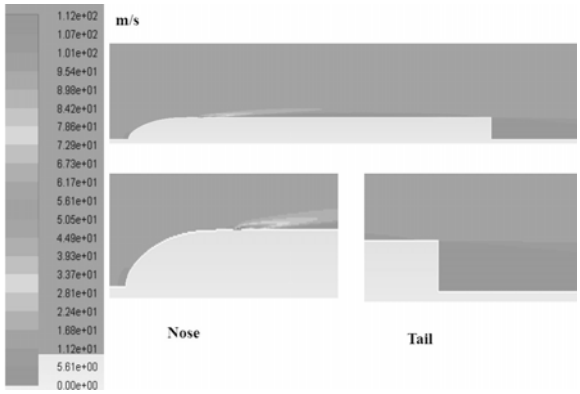

(b) Blunt Afterbody1 (U = 15 m/s and U_{jet} = 50 m/s)

Fig. 12 Velocity contours for Afterbody1 and Blunt Afterbody1 at air jet speeds corresponding to maximum drag reduction.

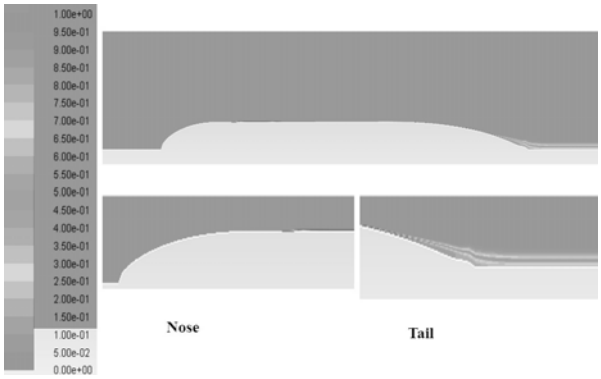

(a) Contour plot for whole domain for Afterbody1 (U = 15m/s and U_{jet} = 1 m/s)

(b) Enlarged view of VF contour near body wall

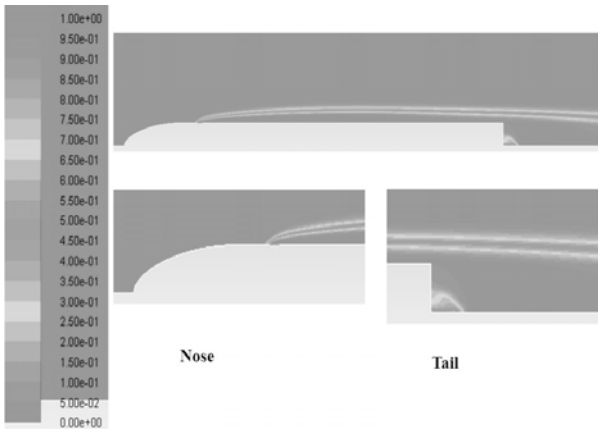

(c) Contour plot for whole domain for Blunt Afterbody1 (U = 15m/s and U_{jet} = 50 m/s)

(d) Enlarged view of VF contour near body wall

Fig. 13 VF contours for Afterbody1 and Blunt Afterbody1 at air jet speeds corresponding to maximum drag reduction.

Variations of molecular viscosity along the length of the body for the air jet velocity at which maximum drag reduction occurs, i.e. U_{jet}≈ 1 m/s for Afterbody1 and U_{jet}≈ 50 m/s for Blunt Afterbody1 are shown in Fig. 14 and volume fraction distributions of water in Fig. 15. Variation of dynamic pressure distribution along the body wall for Afterbody1 is shown in Fig. 16 and that for Blunt Afterbody1 in Fig. 17.

To study the effect of the angle of introduction of the air jet (θ), five values (10, 20, 30, 60 and 90°) were chosen with U = 15 m/s. The results are shown in Fig. 18 and Table 5 for Afterbody1 and in Fig. 19 and Table 6 for Blunt Afterbody1.

To study the effect of velocity of the body on drag reduction, three different values of U (1, 4 and 15

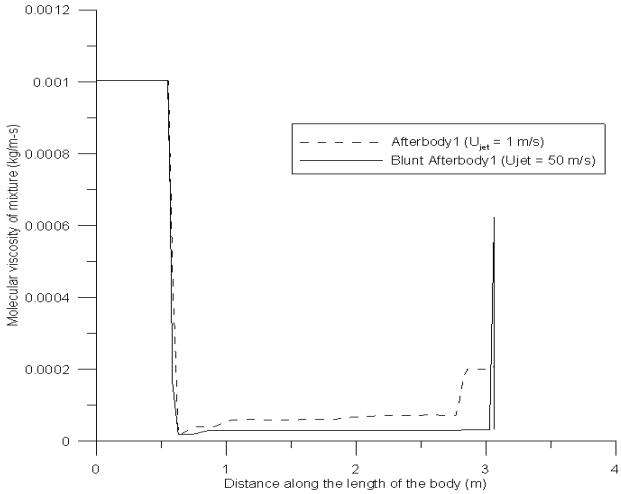

Fig. 14 Comparison of molecular viscosity of mixture along length of body.

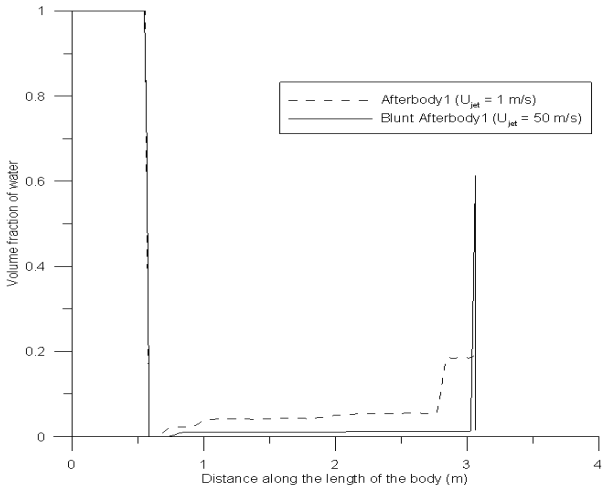

Fig. 15 Comparison of volume fraction of water along length of body.

m/s) have been considered for both bodies. The results are shown in Fig. 20 and Table 7 for Afterbody1 and in Fig. 21 and Table 8 for Blunt Afterbody1.

To study the effect of injecting air jets by discrete air inlets, when the flow problem ceases to be axisymmetric, a 3D CFD simulation is done with four discrete air inlets, each 90° apart, with same total mass flow rate (0.05U kg/s) as in case of axisymmetric studies which imply a ring shaped air inlet. In the axisymmetric geometry, the width of the air jet was 0.05 m, giving a total jet area of 0.043 m^2. In the 3D geometry, the discrete jets had an elliptical shape on the body surface but the total jet area of four jets was the same as that of the ring jet. To bring out the difference between axisymmetric and 3D analysis, the 3D CFD simulation results with a ring air jet with zero angle of attack are compared with the axisymmetric analysis results in Table 9 for

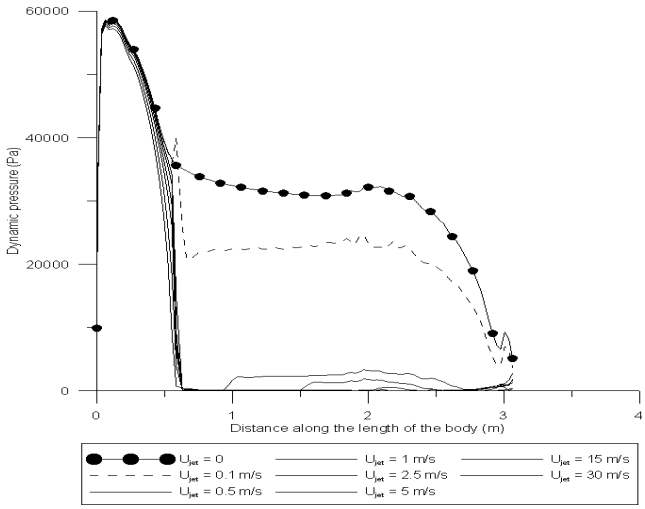

Fig. 16 Dynamic pressure distribution along length of body for different U_{jet} for Afterbody1(U = 15 m/s).

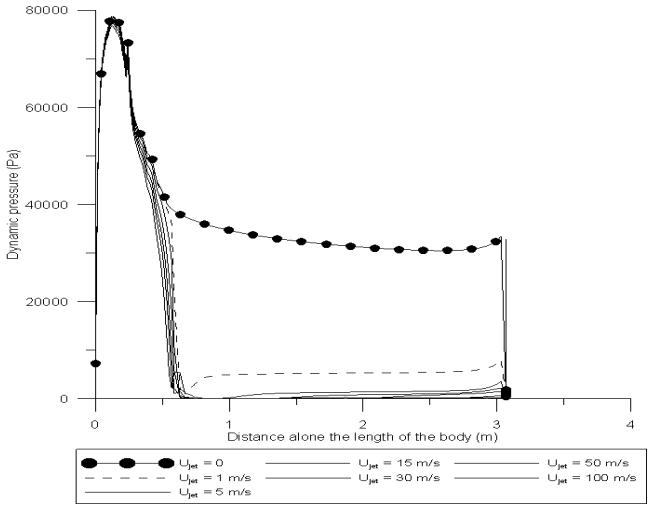

Fig.17 Dynamic pressure distribution along length of body for different U_{jet} for Blunt Afterbody1 (U = 15 m/s).

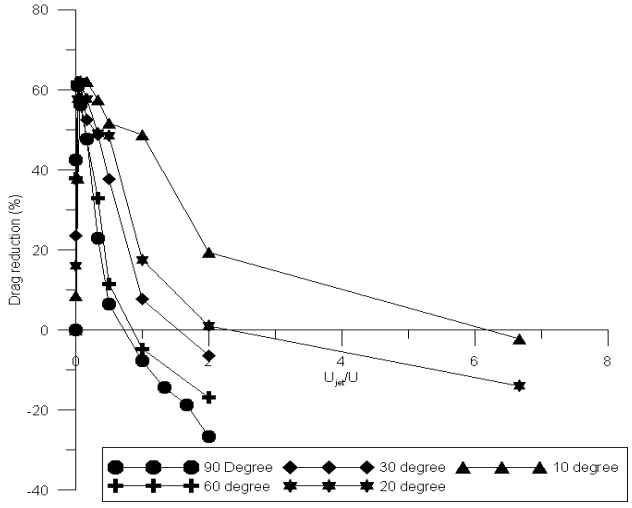

Fig. 18 Influence of angle of injection of air jet on drag reduction for Aferbody1 (U = 15 m/s).

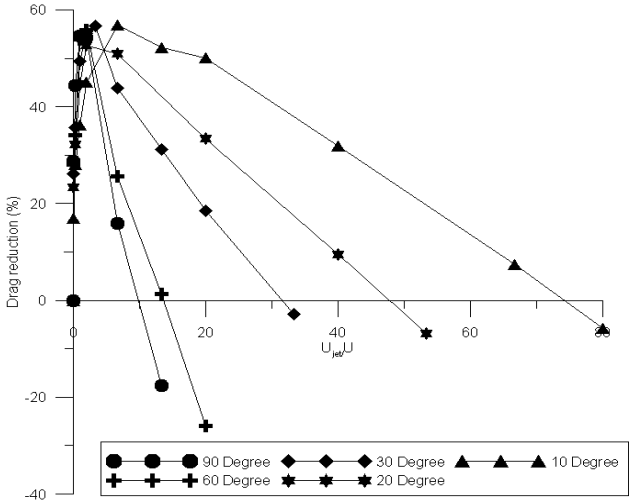

Fig. 19 Influence of angle of injection of air jet on drag reduction for Blunt Aferbody1(U = 15 m/s).

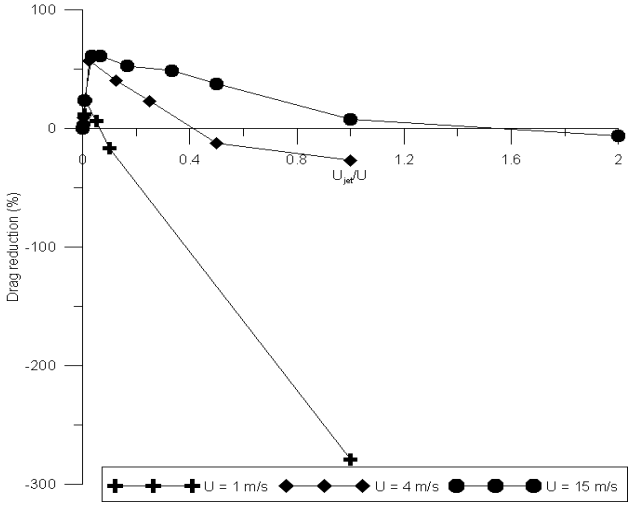

Fig. 20 Influence of velocity of body on drag reduction for Aferbody1.

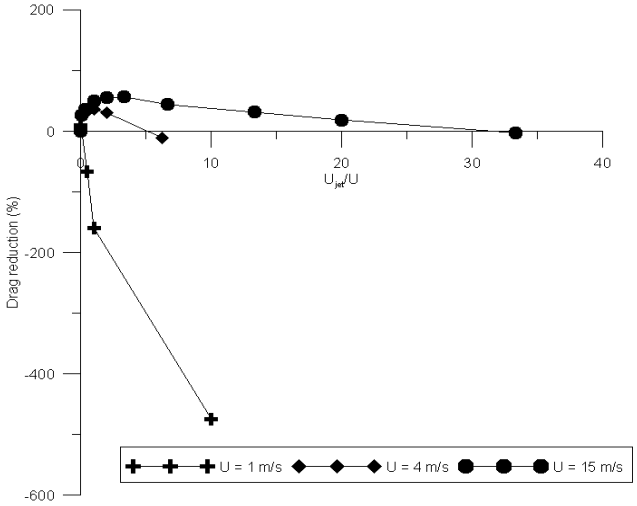

Fig. 21 Influence of velocity of body on drag reduction for Blunt Aferbody1.

Table 5: Drag reduction for various angles of air jet for Afterbody1 (U = 15 m/s, $Re = 4.6\times10^7$).

θ (deg)	U_{jet} (m/s)	F_P (N)	F_F (N)	F_D (N)	Drag reduction (%)
10	0	53.54	589.90	643.44	-
	0.1	52.61	535.18	587.79	8.64
	0.5	50.45	348.89	399.35	37.93
	1	52.05	218.23	270.29	57.99
	2.5	73.44	170.63	244.07	62.06
	5	120.21	153.03	273.25	57.53
	7.5	164.23	146.79	311.02	51.66
	15	188.13	141.46	329.59	48.77
	30	381.62	137.04	518.66	19.39
	100	520.24	137.42	657.67	–2.21
20	0	53.54	589.90	643.44	-
	0.1	51.92	488.32	540.24	16.03
	0.5	52.03	220.44	272.47	57.65
	1	64.21	180.24	244.45	62.00
	2.5	118.79	153.30	272.10	57.71
	5	183.10	144.24	327.34	49.12
	7.5	189.43	141.35	330.78	48.59
	15	393.77	136.59	530.36	17.57
	30	501.75	135.33	637.09	0.98
	100	599.41	134.33	733.74	–14.03
30	0	53	589	643	-
	0.1	51	441	492	23.48
	0.5	56	193	249.9	61.13
	1	79	169	249.4	61.21
	2.5	159	147	306	52.41
	5	188	141	329	48.83
	7.5	263	138	401	37.63
	15	457	136	594	7.62
	30	550	133	684	–6.37
60	0	53.54	589.90	643.44	-
	0.1	50.33	349.67	400.00	37.83
	0.5	73.55	171.83	245.38	61.86
	1	117.97	153.85	271.83	57.75
	2.5	194.07	142.67	336.75	47.66
	5	294.67	137.43	432.11	32.84
	7.5	432.77	136.60	569.38	11.51
	15	540.00	133.71	673.72	–4.70
	30	622.34	130.10	752.44	–16.94
90	0	53	589	643	-
	0.1	50	319	370	42.45
	0.5	79	170	250	61.11
	1	130	151	281	56.29
	2.5	194	141	336	47.74
	5	358	137	496	22.86
	7.5	466	135	602	6.37
	15	559	133	693	–7.77
	20	605	131	736	–14.46
	25	633	129	763	–18.66
	30	689	126	815	–26.74
	50	811	121	932	–44.94
	75	937	115	1052	–63.60
	100	1058	111	1170	–81.95

Table 6 Drag force for various angle of air jet for Blunt Afterbody1 (U = 15 m/s, Re =4.6×10^7).

θ (deg)	U_{jet} (m/s)	F_P (N)	F_F (N)	F_D (N)	Drag reduction (%)
10	0	824.10	684.68	1508.79	-
	1	873.10	379.30	1252.41	16.99
	5	881.88	203.87	1085.75	28.03
	15	799.02	163.01	962.04	36.23
	30	677.59	152.40	829.99	44.98
	100	512.82	137.73	650.55	56.88
	200	564.11	138.17	720.28	52.26
	300	598.47	155.52	753.99	50.02
	600	769.37	257.76	1027.13	31.92
	1000	910.11	485.81	1395.92	7.48
	1200	958.48	636.77	1595.25	–5.73
20	0	824.10	684.68	1508.79	-
	1	889.17	265.97	1155.15	23.43
	5	847.33	176.01	1023.35	32.17
	15	681.86	152.94	834.81	44.66
	30	570.08	144.61	714.7	52.63
	100	614.08	126.31	740.40	50.92
	300	857.47	148.10	1005.57	33.35
	600	1083.78	281.01	1364.79	9.54
	800	1194.75	416.37	1611.12	–6.78
30	0	824	684	1508	-
	1	890	224	1115	26.06
	5	805	164	969	35.74
	15	613	149	762	49.46
	30	539	137	677	55.10
	50	525	128	654	56.63
	100	727	122	846	43.89
	200	914	123	1037	31.23
	300	1100.92	127.20	1228.12	18.55
	500	1406.84	144.18	1551.03	–2.85
60	0	824.10	684.68	1508.79	-
	1	881.36	204.82	1086.19	28.01
	5	825.69	169.02	994.72	34.07
	15	553.84	140.82	694.67	53.95
	30	540.10	126.83	666.93	55.79
	100	1012.29	110.82	1123.12	25.56
	200	14477.65	101.65	1490	1.24
	300	2065.02	97.86	1900	–25.92
90	0	824.10	684.68	1508.79	-
	1	876.78	199.24	1076.03	28.68
	5	686.09	153.10	839.19	44.37
	15	546.51	137.90	684.41	54.63
	30	566.30	123.49	689.80	54.28
	100	1161.68	105.92	1267.61	15.98
	200	1685.08	88.91	1774.00	–17.57

Table 7 Drag force for various body velocities for Afterbody1.

U (m/s)	U_{jet} (m/s)	F_P (N)	F_F (N)	F_D (N)	Drag reduction (%)
1	0	0.34	4.66	5.01	-
	0.001	0.40	4.43	4.84	3.32
	0.005	0.75	3.66	4.41	11.87
	0.01	1.32	2.51	3.84	23.29
	0.05	3.32	1.382	4.70	6.12
	0.1	4.65	1.19	5.85	–16.83
	1	17.40	1.87	19	–279.11
4	0	4.24	50.36	54.62	-
	0.005	4.244	47.62	51.86	5.03
	0.01	4.26	45.38	49.64	9.10
	0.1	5.32	18.16	23.49	56.98
	0.5	19.82	12.86	32.68	40.15
	1	29.72	12.26	41.98	23.13
	2	49.39	12.09	61.49	–12.58
	4	57.02	12.28	69.30	–26.88
15	0	53	589	643	-
	0.1	51	441	492	23.48
	0.5	56	193	249.9	61.13
	1	79	169	249.4	61.21
	2.5	159	147	306	52.41
	5	188	141	329	48.83
	7.5	263	138	401	37.63
	15	457	136	594	7.62
	30	550	133	684	–6.37

Table 8 Drag force for various body velocities for Blunt Afterbody1.

U (m/s)	U_{jet}(m/s)	F_P (N)	F_F (N)	F_D (N)	Drag reduction (%)
1	0	3.48	5.29	8.70	-
	0.001	3.44	5.09	8.53	1.97
	0.005	3.60	4.52	8.13	6.57
	0.01	3.95	3.94	7.90	9.23
	0.5	11.93	2.55	14.49	–66.53
	1	20.43	2.13	22.57	–159.30
	10	72.37	2.52	50	–474.42
4	0	57.27	58.53	115.80	-
	1	65.26	15.53	80.79	30.23
	2	64.47	13.77	78.24	32.43
	4	60.83	12.94	73.78	36.28
	8	68.47	12.35	80.79	30.23
	25	117.38	11.23	128.62	–11.06
15	0	824	684	1508	-
	1	890	224	1115	26.06
	5	805	164	969	35.74
	15	613	149	762	49.46
	30	539	137	677	55.10
	50	525	128	654	56.63
	100	727	122	846	43.89
	200	914	123	1037	31.23
	300	1100.925	127.20	1228.12	18.55
	500	1406.849	144.18	1551.03	–2.85

Table 9 Comparison of drag reduction for zero angle of attack: axisymmetric *vs* 3D analysis (U = 15 m/s, Re = 4.6×10^7) of Afterbody1.

U_{jet} (m/s)	F_P (N)			F_F (N)			F_D (N)			Drag reduction (%)		
	2D	3D*	3D**	2D	3D*	3D**	2D	3D*	3D**	2D	3D*	3D**
0	53.5	58.4	75.6	589	615	606	643	673	681	-	-	-
0.5	79	92.4	75.8	170	208	550	250	301	626	61.1	55.3	8.1
15	559	546	107	133	159	483	693	706	590	–7.8	–4.9	13.4

3D* : 3D analysis result with ring air jet

3D** : 3D analysis result with four discrete air jets, located 90 deg. apart

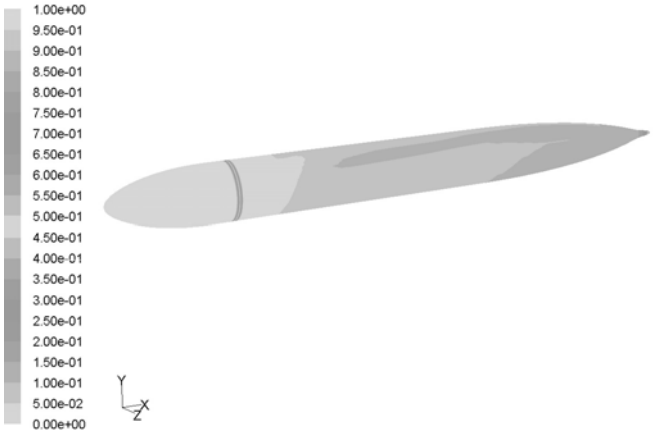

Fig. 22 VF contour of water for ring air jet (U = 15 m/s; U_{jet}= 0.5 m/s).

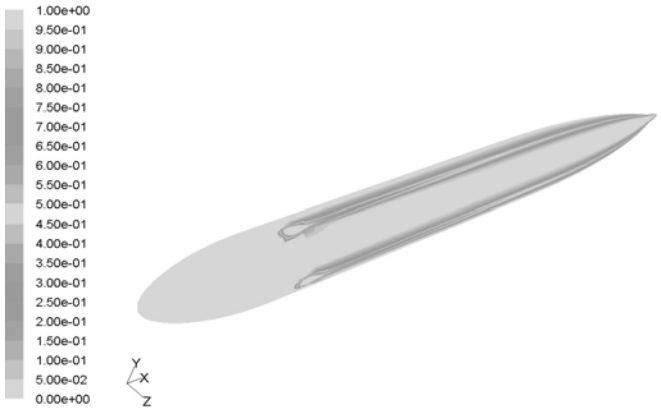

Fig. 23 VF contour of water for four discrete air jets (U = 15 m/s; U_{jet} = 0.5 m/s).

Afterbody1. In this table, the 3D results for the case of four discrete air jets located 90º apart are also given. Figs. 22 and 23 show the contour plots of volume fraction (VF) of the fluid (VF = 1 for water and VF = 0 for air) for two jet configurations with U_{jet} = 0.5 m/s.

To study the effect of nonzero angles of attack on drag reduction, two nonzero angles of attack are considered, α = 5° and 15°, only for a 1:1.9 scaled model of Afterbody1 at U = 4 m/s. The results are shown in Fig. 24 and Table 10.

5.3 Discussion of results

The total drag force consists of two components, namely pressure drag (also called form drag of viscous origin and denoted by F_P) and frictional (viscous) drag (denoted by F_F). The total drag (F_D) is the sum of F_P and F_F. The corresponding drag coefficients (volumetric), denoted C_{PV}, C_{FV} and C_{DV} , are defined as (C_{PV}, C_{FV},C_{DV}) = (F_P, F_F, F_D)/($0.5\rho U^2\nabla^{2/3}$), where ρ is the density of water and ∇ is the volume of the body.

From Table 3, it may be seen that the drag of Blunt Afterbody1 is about 2 times that of Afterbody1 at Re = 6.6×10^6 (U = 2.152 m/s) and about 2.3 times that of Afterbody1 at Re = 4.6×10^7 (U = 15 m/s), indicating a very strong effect of the shape of the stern. This large difference is mainly contributed by the pressure drag. The pressure drag of Blunt Afterbody1 is about 10 times that of Afterbody1 at Re = 6.6×10^6 and about 15 times that of Afterbody1 at Re = 4.6×10^7. This form effect is evident from a comparison of forward and aft pressure distributions on the two bodies (Figs. 9a and 9b). Forward pressures are almost the same for both bodies, however the aft pressures are significantly lower in Blunt Afterbody1 than Afterbody1, thereby creating much larger net force in the forward to aft direction, which is the pressure drag of the body. Figs. 16 and 17 show the dynamic pressure distribution on the Afterbody1 and Blunt Afterbody1, respectively, and they show significantly higher pressures at the forward end in Blunt Afterbody1 than in Afterbody1, once again explaining the significant difference in pressure drag between these two body shapes.

From Table 4 and Fig. 8, it is seen that with increasing air jet velocity, the total drag first decreases (i.e. drag reduction increases as in Fig. 8), reaches a minimum, and then increases again. For Afterbody1, minimum drag is attained when U_{jet}/U is in the range of about 0.5 to 1 (i.e. U_{jet} is in the range of 7.5 to 15 m/s). For Blunt Afterbody1, minimum drag is attained when U_{jet}/U is in the range of about 2 to 3.5 (i.e. U_{jet} in

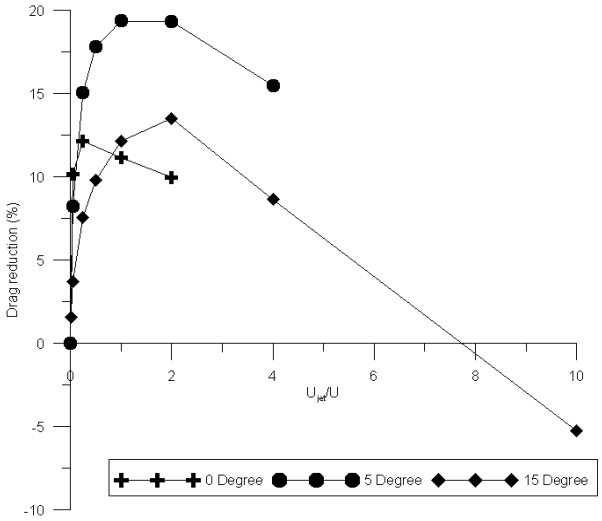

Fig. 24 Influence of angle of attack (α) on drag reduction for 1:1.9 scale model of Aferbody1 at U = 4m/s.

Table 10 Drag reduction for various angles of attack (U = 4 m/s, Re = 6.456×10^6) for 1:1.9 scaled model of Afterbody1.

U_{jet} (m/s)	F_P (N)	F_F (N)	F_D (N)	Drag reduction (%)
0	1.84	16.5	18.4	-
0.2	1.67	14.8	16.5	10.16
1	1.90	14.2	16.1	12.14
4	3.06	13.3	16.3	11.14
8	4.60	11.9	16.5	9.96

(a) $\alpha = 0°$

U_{jet} (m/s)	F_P (N)	F_F (N)	F_D (N)	Drag reduction (%)
0	2.44	16.2	18.6	-
0.2	2.37	14.7	17.1	8.2
1	2.51	13.3	15.8	15.03
2	2.83	12.5	15.3	17.7
4	3.51	11.5	15.07	19.3
8	4.55	10.5	15.08	19.3
16	6.17	9.62	15.80	15.4

(b) $\alpha = 5°$

U_{jet} (m/s)	F_P(N)	F_F(N)	F_D(N)	Drag reduction (%)
0	17.4	19.09	36.2	-
0.04	16.9	18.7	35.6	1.54
0.2	16.7	18.1	34.9	3.67
1	16.6	16.9	33.5	7.57
2	16.6	16.08	32.7	9.76
4	16.9	14.9	31.8	12.1
8	17.8	13.5	31.3	13.5
16	20.6	12.4	33.1	8.62
40	26.5	11.6	38.1	–5.25

(c) $\alpha = 15°$

the range of 30 to 50 m/s). For Afterbody1, at about U_{jet}/U of 2 (i.e. U_{jet} of about 30 m/s), the drag reduction becomes negative (i.e. drag becomes more than that at U_{jet} = 0). However, for Blunt Afterbody1, even at a large U_{jet}/U = 6.67 (U_{jet}= 100 m/s) the drag reduction remains positive (i.e. drag remains less than that at U_{jet} = 0). The nature of the drag reduction curves indicates that drag reduction will remain positive for even higher values of U_{jet} for Blunt Afterbody1. Maximum drag reductions for both bodies are somewhat similar, 61% for Afterbody1 and 57% for Blunt Afterbody1. However, in the case of Afterbody1, large drag reduction is possible within a smaller range of air jet velocities, whereas in the case of Blunt Afterbody1, large drag reduction is possible within a much larger range of air jet velocities. Also, in the case of Afterbody1, large drag reduction occurs at small values of air jet velocity, whereas in the case of Blunt Afterbody1, large drag reduction occurs at much larger values of air jet velocity.

Comparing the pressure distributions in Fig. 9a (U_{jet} = 0) and Fig. 10a (U_{jet} = 1 m/s) for Afterbody1, one can notice that aft pressure is somewhat lower with the air jet than without the air jet. This should lead to higher pressure drag with air jet (79 N with air jet *vs.* 53 N without air jet in Table 7). However, total drag is lower by 61% with the air jet because frictional drag reduces significantly (169 N with air jet *vs.* 589 N without air jet in Table 7). This is because air engulfs the last one-third of the sloping aft region entirely (Figs. 13a and 13b) leading to reduction in frictional drag due to lower air density. This effect of engulfing of the body with air is far more pronounced for Blunt Afterbody1 leading to significant frictional drag reduction (Table 8).

From the variation of molecular viscosity (viscosity of air is 1.789×10^{-5} kg/(m.s) and that of water is 1.003×10^{-3} kg/(m.s)) along the length of the body, as shown in Fig. 14, it is clear that the major reason of drag reduction is the drastic reduction in molecular viscosity along length of the body beyond the location of air jet injection. This causes the reduction in the frictional component of drag force. In all calculations, a major portion of the body surface is covered with a mixture of water and air (Fig. 15) and the content of air in the mixture along the length of the body does not have much variation. Pressure drag was found to initially decrease and then increase with velocity of the air jet. Due to this variation in pressure drag, total drag force also follows the same pattern. Pressure drag is formed

due to the difference in pressure between the forward and aft ends of the body. At higher air jet velocity, the pressure difference between the aft and forward ends of the body increases which cause pressure drag to increase. The volume fraction distribution of water on the aft end shows that at higher air jet velocity, air does not cover the body surface fully, which lowers the pressure in the stern end. In all cases pressure distribution forward of the air jet location remains unaltered (i.e. in the fore body), so that the pressure and volume fraction in the stern essentially determines the magnitude of drag reduction.

Figs. 18 and 19 show that for each angle of injection of the air jet, drag reduction follows the same pattern. The range of the air jet velocity over which reduction happens is quite different for Afterbody1 and Blunt Afterbody1. However, maximum drag reduction remains similar (about 60% for Afterbody1 and about 55% for Blunt Afterbody1) in almost all cases. As the angle decreases, the range of air jet velocities in which drag reduction can be effective is found to increase significantly. For a 10° angle of the air jet, drag reduction can be obtained for Afterbody1 up to $U_{jet} \approx 6U$. For Blunt Afterbody1, however, drag reduction is obtained up to $U_{jet} \approx 70U$.

Figs. 20 and 21 present some results showing the influence of body velocity on drag reduction for various U_{jet}/U ratios. As velocity of the body decreases, the spread of the drag reduction curve also decreases significantly. At lower body velocities, the maximum drag reduction reduces for both bodies. It can be seen that at certain body velocities it may not be practically possible to achieve any drag reduction and on the contrary, drag may increase.

The drastic fall in drag reduction for lower air jet speed, 55% to 8% for $U_{jet} = 0.5$ m/s in case of the four discrete air jets over the case of the ring air jet, is clearly attributable to the fact that in the former case air is not able to cover the surface of the body fully and hence, drag reduction is much lower. This is vividly brought out in Figs. 22 and 23 for two jet configurations for $U_{jet} = 0.5$ m/s.

From Fig. 24 and Table 10, it may be seen that for non-zero angles of attack, the maximum drag reduction is in the range of 10 to 20%, while for the air jet in the form of a ring, the maximum drag reduction was in the range of 50 to 60%, again due to the air not being able to cover the surface of the body fully in the case of air jets. Maximum drag reduction is obtained when velocity of the air jet and angle of the air jet is smaller for higher body speed and for zero angle of attack of the body. For larger angles of attack of the body, the peak of drag reduction curve shifts to higher values of air jet velocity. From the volume fraction plots it was observed that at higher angles of attack and at higher air jet velocities, the air jet gets separated from the body surface, thus reducing drag reduction. The parameters that affect drag reduction are U_{jet}, θ and α. The optimal values of these parameters, in other words, the combination for which drag reduction is maximum, will require many CFD runs which may be worthwhile only when one has reasonable experimental validation and this has not been done in the present work. Even then, the CFD based optimal values may not be always practicable (e.g. too large or too small values of θ) and hence, practical choice of optimal values will require a judicious combination of CFD approach and practicability. Nevertheless, from Tables 5 to 8 and Table 10, it seems that $\theta = 30°$ is a practical optimal choice for both bodies and also in most cases $\alpha = 0°$ gives the best drag reduction. As for U_{jet}, a value of around 0.5 to 2.5 m/s is optimal for Afterbody1 and a value of around 30 to 50 m/s is optimal for Blunt Afterbody1; all for $U = 15$ m/s.

6. CONCLUSIONS

A computational fluid dynamics approach for estimation of drag reduction using air jets for underwater axisymmetric vehicles has been presented and reasonably validated with other numerical work. Maximum drag reduction can be obtained if the influencing parameters are selected in their optimal ranges. Drag reduction with air jets has been demonstrated to be an effective potential method of drag reduction. Experimental validation is required for further meaningful research in this area.

REFERENCES

1. Ali D, Yasemin A, Fahri C (2010). A numerical investigation of air lubrication effect on ship resistance. *International Conference on Ship Drag Reduction SMOOTH-SHIPS*. Istanbul, Turkey.
2. Deutsch S, Castano J (1985). *Microbubble Skin Friction Reduction on an Axisymmetric Body*. Technical memorandum (N00024-79-C-6043), The Pennsylvania State University, USA.
3. Fontaine AA, Deutsch S (1992). The influence of the type of gas on the reduction

of skin friction drag by microbubble injection. *Experiments in Fluids* 13:128-136.
4. Hassan AY, Claudia C, Gutierrez T, Jose AJB (2005). Temporal correlation modification by microbubbles injection in a channel flow. *International Communication in Heat and Mass Transfer* 32:1009-1015.
5. Huang TT, Santelli N, Belt G (1978). Stern boundary-layer flow on axisymmetric bodies. *Twelfth Symposium on Naval Hydrodynamics*. Washington, 125-167.
6. Jagadeesh P, Murali K (2006). Investigation of alternative turbulence closure models for axisymmetric underwater bodies. *Maritime Emergency Management* 1(2):37-57.
7. John D, Roger NH, Marc S, Poul SL (2011). Drag reduction by air release promotes fast ascent in jumping emperor penguins-a novel hypothesis. *Marine Ecology Progress Series* 430:171-182.
8. Kanai A, Miyata H (2001). Direct numerical simulation of wall turbulent flows with microbubbles. *International Journal for Numerical Methods in Fluid* 35:593-615.
9. Kato H, Iwashina T, Miyanaga M, Yamaguchi (1999). Effect of microbubbles on the structure of turbulence in a turbulent boundary layer. *Journal of Marine Science and Technology* 4:155-162.
10. Kim SY, Cleaver WJ (1995). The persistence of drag reduction following the injection of microbubbles into turbulent boundary layer. *International communications in Heat and Mass Transfer* 22:353-357.
11. Kodama Y, Kakugawa A, Takahashi T, Kawashima H (2000). Experimental study on microbubbles and their applicability to ships for skin friction reduction. *International Journal of Heat and Fluid Flow* 21:582-588.
12. Madavan NK, Deutsch S, Merkle CL (1984). Reduction of turbulent skin friction by microbubbles. *Physics of Fluids* 27(2):356-363.
13. Madavan NK, Deutsch S, Merkle CL (1985). Measurements of local skin friction in a microbubble-modified turbulent boundary layer. *Journal of Fluid Mechanics* 156:237-256.
14. Manninen M, Taivassalo V, Kallio S (1996). *On the Mixture Model for Multiphase Flow*. VTT Publications 288, Finland.
15. Mohanarangam K, Cheung SCP, Tu JY, Chen L (2009). Numerical simulation of micro-bubble drag reduction using population balance model. *Ocean Engineering* 36:863-872.
16. Moriguchi Y, Kato H (2002). Influence of microbubble diameter and distribution on frictional resistance reduction. *Journal of Marine Science and Technology* 7:79-85.
17. Murai Y, Fukuda H, Oishi Y, Kodamaand YF (2007). Skin friction reduction by large air bubbles in a horizontal channel flow. *International Journal of Multiphase Flow* 33:147-163.
18. Sarkar T, Sayer PG, Fraser SM (1997). Flow simulation past axisymmetric bodies using four different turbulence models. *Applied Mathematical Modelling* 21:783-792.
19. Skudarnov PV, Lin CX (2006). Drag reduction by gas injection into turbulent boundary layer: Density ratio effect. *International Journal of Heat and Fluid Flow* 27:436-444.
20. Truong VT (2001). *Drag Reduction Technologies*. Report, DSTO Aeronautical and Maritime Research Laboratory, Australia. DSTO-GD-0290.
21. Virag M, Vengadesan S, Bhattacharyya SK (2011). Translational added mass of axisymmetric underwater vehicles with forward speed using computational fluid dynamics. *Journal of Ship Research* 55(3):185–195.
22. Wedin R, Davoust L, Cartellier A, Byrne P (2003). Experiments and modelling on electrochemically generated bubbly flows. *Experimental Thermal and Fluid Science* 27:685-696.
23. Wu C, He S, Zhu D, Gu M (2006). Numerical simulation of microbubble flow around an axisymmetric body. *Journal of Hydrodynamics* 18(3):217-222.
24. Wu S, Cheng HH, Tsung TL (2005). Model test of the surface and submerged vehicles with the micro-bubble drag reduction. *Ocean Engineering* 34(1):83-93.
25. Wu SJ, Kwan O, Shiah SW (2008). Robust design of microbubble drag reduction in a channel flow using the Taguchi method. *Ocean Engineering* 35:856-863.
26. Xiang M, Zhang W, Cheung SCP, Tu J (2012). Numerical investigation of turbulent bubbly wakes created by the ventilated partial cavity. *Science China* (*Physics, Mechanics and Astronomy*) 55(2):297-304.